Am J Cancer Res 2024;14(8):3976-3993
www.ajcr.us /ISSN:2156-6976/ajcr0157340

Original Article

Targeted multimodal synergistic therapy of drug-resistant HER2-positive breast cancer by pyrotinib-ICG self-assembled nanoparticles

Juncheng Xuhong[1,3*], Nisha Wu[1*], Qiyun Shi[1,4], Hao Tian[1], Zaihui Peng[1], Jun Jiang[1], Jing Zhang[2], Xiaowei Qi[1]

[1]Department of Breast and Thyroid Surgery, Southwest Hospital, Army Medical University, Chongqing 400038, China; [2]Department of Laboratory Medicine, Nanfang Hospital, Southern Medical University, Guangzhou 510515, Guangdong, China; [3]Shigatse Branch, Xinqiao Hospital, Third Military Medical University, Shigatse 857000, Xizang, China; [4]The Eighth Medical Center, Chinese PLA General Hospital, Beijing 100091, China. [*]Equal contributors.

Received April 22, 2024; Accepted August 7, 2024; Epub August 25, 2024; Published August 30, 2024

Abstract: Neoadjuvant targeted therapy combining targeted agents with chemotherapy significantly improve survival rates of patients suffering from human epidermal receptor (HER2)-positive breast cancer (BC) in early or locally advanced stages. However, approximately 50% of patients fail to achieve a pathological complete response. In response, targeted photothermal therapy (PTT) and photodynamic therapy (PDT) have emerged as effective strategies to bolster primary tumors treatment. In this context, we developed a novel nanodrug, referred to as "P/ICG", which comprised of a tyrosine-kinase inhibitor pyrotinib and the photosensitizer indocyanine green (ICG). This formulation was created for the targeted and multimodal synergistic therapy of HER2-positive BC. Upon irradiation with near-infrared light, ICG generates high levels of intracellular reactive oxygen species and elevated temperature, enhancing chemotherapy effects of pyrotinib. This synergistic action boosts a highly effective anticancer effect promoting the ferroptosis pathway, providing an efficient therapeutic strategy for treating HER2-positive BC.

Keywords: HER2-positive breast cancer, photothermal therapy, photodynamic therapy, pyrotinib, indocyanine green

Introduction

Breast cancer (BC) is one of the most prevalent malignant tumors threating women's health [1]. In China, the incidence of breast cancer has been increasing annually, gradually aligning with rates observed in developed countries [2]. Among the factors contributing to mortality in Chinese women with BC, obesity is the largest contributor, followed by smoking and high intake of red meat [3]. Integrated multiomic profiling has illustrated that HER2-enriched subtype breast cancer is remarkably high in Chinese population, characterized by frequent ERBB2 amplification and higher HER2 protein abundance [4]. Human epidermal receptor (HER) 2, a member of epidermal growth factor receptor (EGFR) family, is overexpressed or amplified in approximately 15-20% of all BC cases, which is strongly associated with aggressive tumor phenotype and poor prognosis [5-8]. HER2-targeted therapy, as the main strategy for HER2-positive BC, has improved survival and prognosis of patients [9, 10]. However, some patients have inherent resistance or acquired resistance to HER2-targeted drugs, which often lead to poor effects of targeted drugs and minimal tumor regression [11, 12]. Moreover, after receiving HER2-targeted neoadjuvant therapy, over 50% of patients with HER2-positive BC fail to achieve a pathological complete response [13-15], which correlates with a decline in long-term progression-free survival [16-18].

PTT and PDT have been postulated to consolidate the local treatment of solid tumors [19, 20], as they cannot induce systemic reactions and cause minimal damage to surrounding normal tissues [21, 22]. Indocyanine green (ICG), a fluorescent tracer used in the clinic, has an

https://doi.org/10.62347/JZRN6919

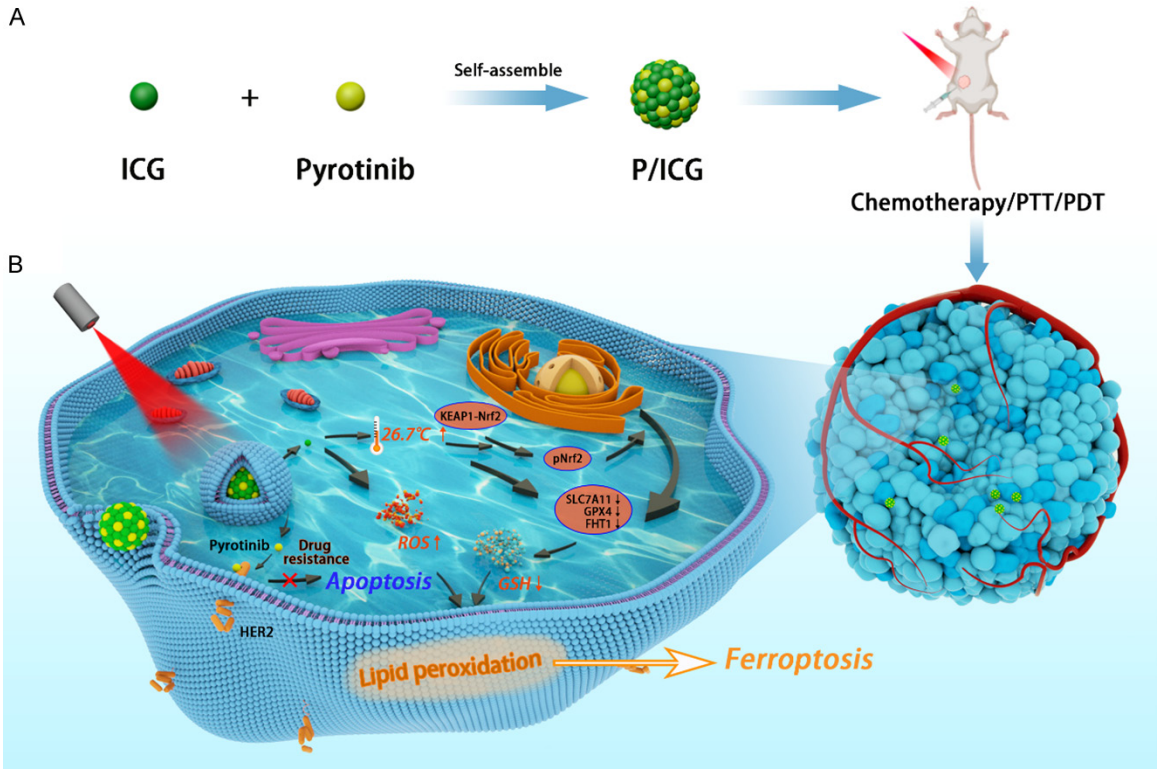

Figure 1. Self-assembled nanoparticles P/ICG for HER2-targeted photothermal therapy and photodynamic therapy. A. Self-assembled nanodrug comprising ICG and pyrotinib. B. Anti-tumor therapy using P/ICG to induce ferroptosis (schematic).

absorption peak in the near-infrared light (NIRL) region and exhibits remarkable photothermal and photodynamic effects [23-26]. However, the complete eradication of solid tumors solely by PTT or PDT is challenged by three primary limitations of ICG: (i) lack of selectivity to malignant cells; (ii) the efficiency of PTT and PDT being heavily dependent on the light source; (iii) the concentration of ICG solution and the properties of the solvent critically influencing its absorption characteristics [27, 28].

Pyrotinib is a novel pan EGFR family tyrosine kinase inhibitor [29-32], with several studies underscoring its high safety and efficacy in the treatment of HER2-positive advanced BC [33-38]. Given the challenges of ICG in terms of targeting and dependence on light sources, we developed a nanodrug named "P/ICG" by integrating ICG and pyrotinib, which can solve the limitation of ICG (**Figure 1A**) and exert a synergistic and highly effective anti-cancer outcome. Our findings indicate that P/ICG specifically targets HER2-positive BC cells, accumulating pyrotinib and ICG within cytoplasm (**Figure 1B**). Moreover, when combined with NIRL irradiation, P/ICG exhibited significant anti-tumor capacity in a model of pyrotinib-resistant BC by alleviating ferroptosis, switching the balance of reactive oxygen species (ROS) and glutathione, and reinforcing lipid peroxidation [39-41]. Our research provides a novel comprehensive strategy for the treatment of HER2-positive BC via multimodal collaborative approaches.

Materials and method

Materials and instruments

Pyrotinib was provided by Jiangsu Hengrui Medicine (Jiangsu, China). ICG was purchased from J&K Chemicals (Shanghai, China). Ferrostatin-1 and liproxstatin-1 were obtained from MedChemExpress (Monmouth Junction, NJ, USA). The reagents including DCFH-DA probe, 4',6-diamidino-2-phenylindole, MDA testing kit, and phenylmethanesulfonylfluoride were sourced from Beyotime Institute of Biotechnology (Shanghai, China). The cell culture reagents including PBS, RPMI 1640 medi-

um, fetal bovine serum, penicillin-streptomycin solution, and trypsin-EDTA solution were obtained from Hyclone (Logan, UT, USA). Methanol, ethanol, and isopropanol were purchased from Chongqing Chuandong Chemicals (Chongqing, China).

Cell lines

BT474 cells, sourced from American Tissue Culture Collection in Manassas, VT, USA, were cultured in RPMI 1640 medium containing 10% fetal bovine serum, 1% penicillin and 1% streptomycin. The primary cell line BREB1, derived from the tumor tissues of patients with HER2-positive BC and harboring the H1047L mutation of PIK3CA, is characterized by low adhesion. BREB1 cells were cultured using a specialized primary BC cell-culture medium purchased from Precedo Biomedical Technology (D12108C). The cells were maintained at 37°C in 5.0% CO_2 atmosphere within a cell incubator.

Animals

The study protocol was approved by the Ethics Committee of our institution. Female NOD-SCID mice, aged 6 weeks, were purchased from Beijing Charles River Laboratories (Beijing, China).

Preparation of P/ICG

ICG-loaded nanoparticles were synthesized by ICG-templated self-assembly of small-molecule drugs. First, 645 μL of a dimethyl-sulfoxide solution of pyrotinib (1 mg/mL) was added into 2 mL of an aqueous solution of ICG (1.0 mg/mL) at a molar ratio of 0.5:1. The mixture was continuously stirred for 20 minutes before being centrifuged at 15,000× *g* for 30 minutes at room temperature to collect the particles. These were resuspended in the aqueous solution and purified from free drugs by ultracentrifugation using a 10 kDa cutoff ultrafiltration centrifuge tube.

Characterization of P/ICG

The hydrodynamic diameter and zeta potential of nanoparticles were measured using a nanoparticle size analyzer (ZetasizerNano ZSP, Malvern, UK) by using DLS technology to measure the particle size and distribution. Electrophoretic light scattering (ELS) was used to measure the electrophoretic mobility and charge (Zeta potential) of molecules or particles in the dispersion system, and static light scattering (SLS) was employed to analyze the molecular weight of particles in the solution. The morphology of nanoparticles was examined by a TEM (FEI Tecnai F20, Thermo, USA). The mass and proportion of N, C, H, and S elements of nanoparticles and the drug-loading proportion of ICG and pyrotinib were measured by an organic element analyzer (Vario EL cube, Elementar, Germany). Then, the absorption and fluorescence spectrum of ICG and the nanoparticle suspension were recorded by a fluorescence/UV-visible spectrophotometer (LS-55, Perkin Elmer, USA). The short-term stability of the nanoparticles was evaluated by the nanoparticle size analysis.

Cellular uptake in vitro

BT474 or BREB1 cells were seeded at 1×10^4/well in a 3-mm confocal dish and treated with ICG and P/ICG at a concentration of 0.2 mg/mL after 24 h. Cells were fixed with paraformaldehyde for 15 minutes at various times (1, 2, 4, 8, 12 and 16 hours) followed by staining with 4',6-diamidino-2-phenylindole for 5 minutes. An anti-fluorescence quenching agent (P0128, Beyotime, China) was then applied. Cells were photographed using a confocal laser scanning microscope (ZISS 880, ZEISS, Germany). Intracellular fluorescence was quantified by flow cytometry using an ACEA NovoCyte system.

Antitumor effect in vitro

BT474 or BREB1 cells were seeded at a density 5,000-10,000 cells/well in a 96-well plate. After 24 hours, the original culture medium was replaced with culture medium containing PBS, ICG, P/ICG (100 μL/well), setting three replicates for each group. Following another 24-hour period, cells were irradiated with NIRL. Subsequently, 10 μL of CCK8 solution was added to each well, including a cell-free medium blank control. After 2 hours, absorbance at 450 nm was measured by enzyme-labeled instrument (Thermofisher, USA).

Detection of photothermal effect and calculation of photothermal conversion efficiency

P/ICG solution (0.5 mL at 0.2 mg/mL) was placed in a 48-well plate with a thermometer

inserted. After stabilizing to room temperature, the solution was irradiated the with 808 nm near-infrared light at different power densities of 0, 0.5, 1.00 and 1.50 W/cm^2 for 300 seconds to monitor the temperature changes and assess photothermal conversion efficiency. Additional tests involved different concentrations P/ICG solutions (0, 0.1 and 0.2 mg/mL) in a transparent cuboid sample pool, irradiated with 1.0 W/cm^2 near infrared light, with temperatures recorded every 30 seconds using an infrared thermal imager. In order to measure the photothermal conversion efficiency, 0.2 mg/mL P/ICG was irradiated at 1.0 W/cm^2 808 nm for 5 minutes, then the irradiation was removed and cooled to room temperature. During this process, the temperature of the solution was recorded every 30 seconds. The photothermal conversion efficiency of P/ICG was measured with reference to previous literature [24].

ROS measurement in vitro

BT474 or BREB1 cells (1×10^4/well) were cultured in a 3-mm confocal dish and treated with ICG or P/ICG at 0.2 mg/mL. After 24 h, cells were irradiated with an 808-nm laser at a power density of 1.0 W/cm^2 for 5 minutes. After irradiation, cells were stained with DCFH-DA to detect ROS and imaged using a confocal microscope. Intracellular DCF levels was quantified *via* flow cytometry.

Antitumor effect in vivo

The antitumor efficacy of P/ICG combined with NIRL irradiation was evaluated using a BREB1 cell-based tumor model in mice, under a protocol approved by the Ethics Committee of Southwest Hospital in accordance with the guidelines for the Use of Laboratory Animals. BREB1 tumors was implanted into the fourth left fat pads of NOD-SCID mice. The long diameter (L) and short diameter (W) of the tumors were measured and tumor volume (V) was calculated as (L × W × W)/2. Once the tumor volume reached 100 mm^3, mice were randomly divided into five groups, each consisting of five mice. In the experimental group, mice were injected with ICG or P/ICG at a dosage of 0.02 mg/kg body weight. One-hour post-injection, the tumors were irradiated with 808 nm NIRL at a power density of 1.0 W/cm^2 for 5 minutes. Mice were photographed by an infrared thermal imager (FLIR E40, FLIRSystems, USA) every minute from radiation initiation. The temperature of the irradiated site was recorded.

Over a 2-week observation period, the weight and volume of the tumor were measured. Post-observation, tumor and vital organs (heart, liver, spleen, lungs, kidneys) were harvested. The weight and size of the tumor were measured. Tissues were then fixed with 4% paraformaldehyde for 24 hours, processed into paraffin sections, and subjected to H&E staining histopathological examination.

In addition, survival data were collected from the same five groups (n = 5). The study documented mortality rates and specific causes of death, such as tumor ulceration or excessive tumor growth exceeding 1,000 mm^3, to evaluate the long-term effects of the treatment.

MDA measurement

BT474 and BREB1 cells were co-cultured with ICG and P/ICG at a concentration of 0.2 mg/mL. After 24 hours, cells were exposed to an 808-nm laser at a power density of 1.0 W/cm^2 for 5 minutes. Cells were then collected and lysed with RIPA. Thiobarbituric acid was added to the lysis solution and combined with MDA to produce a red adduct at 100°C. The absorbance of this adduct was measured at 535 nm to determine MDA levels.

Western blotting

BREB1 cells were washed twice with PBS and lysed in RIPA buffer. Following cryogenic centrifugation, proteins were collected into an Eppendorf™ tube. Then, 5× SDS-PAGE Protein Loading Buffer was added into the lysates, which were then agitated and heated at 100°C for 10 minutes. Total proteins were separated by sodium dodecyl sulfate-polyacrylamide gel electrophoresis (SDS-PAGE) and transferred to polyvinylidene fluoride (PVDF) membranes. Then, PVDF membranes were marked and blocked with 5% milk solution for 1 hour at room temperature, washed four times with TBST (Tris-buffered saline and Tween-20), and incubated overnight at 4°C with primary antibodies against Nrf2, p-Nrf2, KEAP1, SLC7A11, GPX4, FTH1, and β-actin (1:2,000 dilution; Cell Signaling Technology). Horseradish peroxidase-conjugated secondary antibodies (1:2,000 dilu-

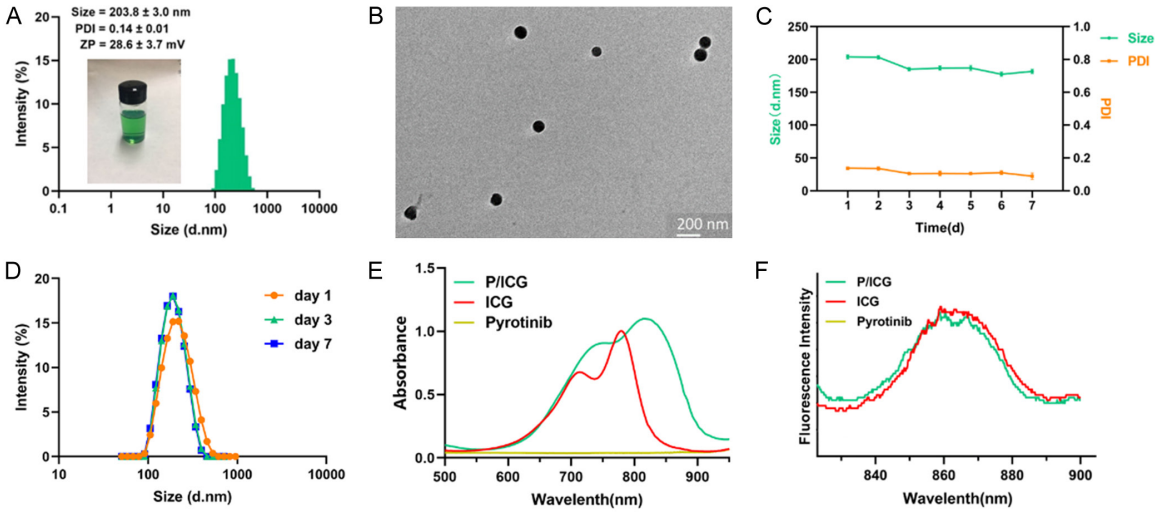

Figure 2. Characterization of P/ICG. A. DLS of P/ICG. B. Morphology of P/ICG under TEM (scale bar = 200 nm). C. Continuous measurement of the particle size and PDI of P/ICG for 1 week. D. DLS of P/ICG at days 1, 3, and 7. E. Absorption spectrum. F. Fluorescence spectrum.

tion; Cell Signaling Technology) were applied subsequently. The PVDF membranes were then processed with chemiluminescent substrate and imaged by a gel-imaging system (ChemiDoc XRS$^+$; Bio-Rad Laboratories, Hercules, CA, USA).

RNA-sequencing

Total RNA was extracted from BREB1 cells treated with PBS, P/ICG, or P/ICG + L using TRIzol® Reagent (Thermo Fisher Scientific, USA) in triplicate. RNA purification, reverse transcription, library construction, and sequencing were performed at Shanghai Majorbio Biopharm Biotechnology (Shanghai, China). According to the TruSeq™ RNA Sample Preparation Kit of Illumina (San Diego, CA, USA), total RNA (1 μg) was used to prepare a transcriptome library. In brief, messenger-RNA was isolated using oligo(dT) beads and fragmented. Double-stranded complimentary cDNA was synthesized by a random hexamer primer (Illumina) and the SuperScript Double-Stranded cDNA Synthesis Kit (Invitrogen, Carlsbad, CA, USA). Following terminal repair, phosphorylation, and addition of the "A" base, cDNA was size-selected on a 2% low-range ultra agarose gel to isolate a 300 bp target fragment. The library underwent 15 polymerase chain reaction cycles using Phusion® DNA polymerase (New England Biolabs, Ipswich, MA, USA) and was quantified by a mini fluorometer (TBS380; Promega, Fitchburg, WI, USA). Sequencing was performed on a NovaSeq 6000 sequencer (Illumina), generating paired-end reads of 150 bp.

Results

Preparation and characterization of P/ICG nanodrug

Anticipating the potential of designed nanodrug to target tumor cells, we synthesized the P/ICG nanoparticles using pyrotinib and ICG. First, 645 μL of a dimethyl sulfoxide solution of pyrotinib (1 mg/mL) was dropped into 2 mL of an aqueous ICG solution (1.0 mg/mL). The mixture was subjected to continuous oscillation, followed by centrifugation and ultrafiltration, yielding a purified aqueous solution of P/ICG.

Subsequent freeze-drying and analysis of organic components determined the molar loading of pyrotinib and ICG at approximately ~13.475% and ~86.525%, respectively. Dynamic light scattering (DLS) revealed that the particle size of P/ICG was 203.8 ± 3.0 nm with a polydispersity index (PDI) of 0.14 ± 0.01, and a surface charge was 28.6 ± 3.7 mV (**Figure 2A**). Transmission electron microscopy (TEM) confirmed that P/ICG particles were uniformly sized and spherical in shape (**Figure 2B**).

Continuous monitoring of particle size and PDI over 1 week confirmed the short-term stability

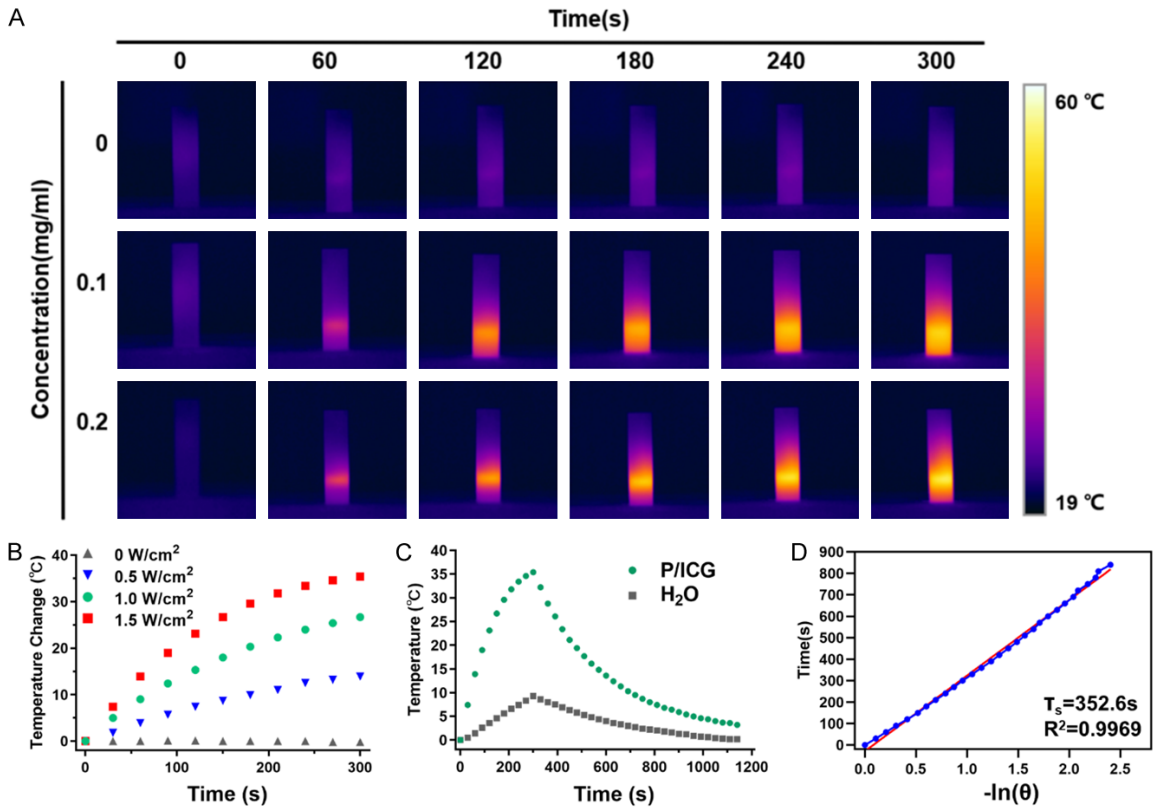

Figure 3. Photothermal effect of P/ICG. A. Infrared thermal images of water and an aqueous solution of P/ICG at different concentrations. B. Temperature *versus* time curve of an aqueous solution of P/ICG (0.1 mg/mL) irradiated by a 808-nm laser at different power densities. C. Cooling curve of water and an aqueous solution of P/ICG (0.1 mg/mL) irradiated by near-infrared light at a power density of 1.0 W/cm^2. D. Plot of time *versus* -ln(θ).

of P/ICG (**Figure 2C** and **2D**). The absorption light spectrum showed that the maximum absorption peak of P/ICG shifted from 775 nm for ICG to 815 nm. The fluorescence spectrum demonstrated that the fluorescence peaks of P/ICG and ICG was approximately 60 nm, respectively (**Figure 2E** and **2F**).

Photothermal effect of P/ICG

The photothermal capabilities of P/ICG was evaluated at varying concentrations and different irradiation conditions using an 808-nm NIR light. Upon irradiation, the temperature of the P/ICG solution increased rapidly, peaking at approximately 5 minutes. Higher concentrations of P/ICG achieved a higher peak temperature (**Figure 3A**). Specifically, at a power density of 0.5 W/cm^2, the temperature of the P/ICG solution increased by approximately 13.9°C. At 1.0 W/cm^2, the temperature of the P/ICG solution increased by ~26.7°C, and at 1.5 W/cm^2, it was around 35.4°C (**Figure 3B**).

To evaluate the efficiency of photothermal conversion, the P/ICG solution was exposed to an NIRL at a power density of 1.0 W/cm^2 until it reached its maximum temperature and was then allowed to cool to room temperature. The temperature changes were meticulously recorded (**Figure 3C**). The efficiency of photothermal conversion was calculated to be approximately 31.945% with a cooling time τ_s = 352.6 s (**Figure 3D**).

When the power density was 1.0 W/cm^2, the temperature of the P/ICG solution increased rapidly and uniformly, whereas the temperature of the water did not increase significantly. Consequently, a power density of 1.0 W/cm^2 was selected for subsequent cell experiments.

Cellular uptake, photodynamic toxicity, and cellular toxicity of P/ICG in vitro

Cellular uptake of P/ICG *in vitro* was evaluated in BT474 and BREB1 cells. BREB1 cells, purified

primary cancer cells derived from patients with HER2-positive BC, harbor the PIK3CA-H1047L mutation, confirmed by next-generation sequencing (**Figure 4A**). These cells, capable of suspension growth in a specifized medium for primary cancer cells, showed stable proliferation (Figure S1). BT474 and BREB1 cells were co-cultured with ICG or P/ICG at 0.2 mg/mL for varying durations (1, 2, 4, 8, 12, and 16 hours). Following fixation, cells were photographed using an ultra-high-resolution confocal laser scanning microscope. Intracellular fluorescence was compared *via* flow cytometry. BT474 cells reached a peak of P/ICG uptake at 12 hours, with uptake rates 1.59 times higher than ICG ($P < 0.0001$). BREB1 cells reached peak uptake at 8 hours, with rates 1.42 times that of ICG ($P = 0.0382$) (**Figure 4B** and **4C**), suggesting effective uptake of P/ICG by HER2-positive BC cells.

Next, we irradiated P/ICG with 808-nm NIRL to induce the generation of ROS. A dichlorodihydrofluorescein diacetate (DCFH-DA) probe was applied to evaluate ROS levels, which converted into green fluorescent DCF upon oxidation. Cells were treated with P/ICG or ICG at a concentration of 2.0 μg/mL for 12 hours before irradiation with 808-nm NIRL for 5 minutes at a power density of 1.0 W/cm^2. Confocal laser scanning microscopy revealed brighter red and green fluorescence in cells treated with P/ICG and NIRL irradiation. The fluorescence intensity of DCF significantly increased after P/ICG was combined with NIRL radiation, indicating elevated ROS levels (**Figure 4D-G**). Quantitative analysis revealed significant increases in ROS in the P/ICG + L group compared to other groups (e.g., BT474 cells: 86.04 ± 8.078 in the ICG group, 108.3 ± 20.29 in the ICG + light (L) group, 102.0 ± 5.558 in the P/ICG group, 187.6 ± 7.446 in the P/ICG + L group; P/ICG + L *vs*. ICG + L, $P = 0.0352$; P/ICG + L *vs*. P/ICG, $P = 0.0058$; BREB1 cells: 24.56 ± 7.080 in the ICG group, 62.96 ± 11.23 in the ICG + L group, 45.52 ± 15.02 in the P/ICG group, 252.1 ± 46.04 in the P/ICG + L group; P/ICG + L *vs*. ICG + L, $P = 0.0009$; P/ICG + L *vs*. P/ICG, $P = 0.0008$). These results confirm the potent photodynamic effect of P/ICG.

The cytotoxic effects of ICG, pyrotinib, and P/ICG combined with NIRL irradiation were evaluated on BT474 and BREB1 cells *in vitro*. Pyrotinib alone had an obvious toxic effect on BT474 cells, with a half-maximal inhibitory concentration (IC_{50}) of 7.487 nmol/L (**Figure 4H**). In contrast, BREB1 cells had strong resistance to pyrotinib, with an IC_{50} of 471.1 nmol/L (**Figure 4I**). Combination treatment with P/ICG and NIRL irradiation markedly reduced cell viability, underscoring the synergistic anti-tumor effects of P/ICG through PTT, PDT, and chemotherapy, particularly in pyrotinib-resistant cells.

Fluorescence imaging in vivo

To investigate the distribution and retention of nanodrugs in tumors, we established a human tumor cell-derived xenograft model using BREB1 cell-derived tissue transplanted into the fat pads of NOD-SCID mice. This local injection method ensures intertumoral enrichment of nanodrugs while minimizing uptake and metabolism by other organs, such as the liver.

BREB1 tumor-bearing NOD-SCID mice were divided into three groups and subjected to local injection of either phosphate-buffered saline (PBS), free ICG, or P/ICG. Following the injection at ICG (0.5 mg/kg bodyweight), the fluorescence signal was measured at various time intervals (**Figure 5A**). The fluorescence intensity for both the ICG group and P/ICG group increased, peaking around 2 hours post-injection before stabilizing with small fluctuations (**Figure 5B**). Twenty-four hours after injection, the mice were euthanized, and their organs were harvested for *ex vivo* fluorescence imaging (**Figure 5C**). This imaging confirmed that fluorescence signals were predominantly localized in tumors, with the mean fluorescence intensity of the P/ICG group being 3.03-fold higher than that of the ICG group ($P < 0.0001$) (**Figure 5D**). Notably, neither free ICG nor P/ICG showed significant accumulation in non-targeted organs.

Antitumor effect of P/ICG in vivo

Next, we evaluated the antitumor effects of P/ICG *in vivo* using a human tumor cell-derived xenograft model as stated above (**Figure 6A**). Fourteen days post-implantation, when the tumor volume reached approximately 100 mm^3, the therapeutic trials commenced. Mice were divided into five groups, each containing five animals: control, ICG, P/ICG, ICG + L, and P/ICG + L. Based on the ICG concentration, the drug was administered directly into the tumors

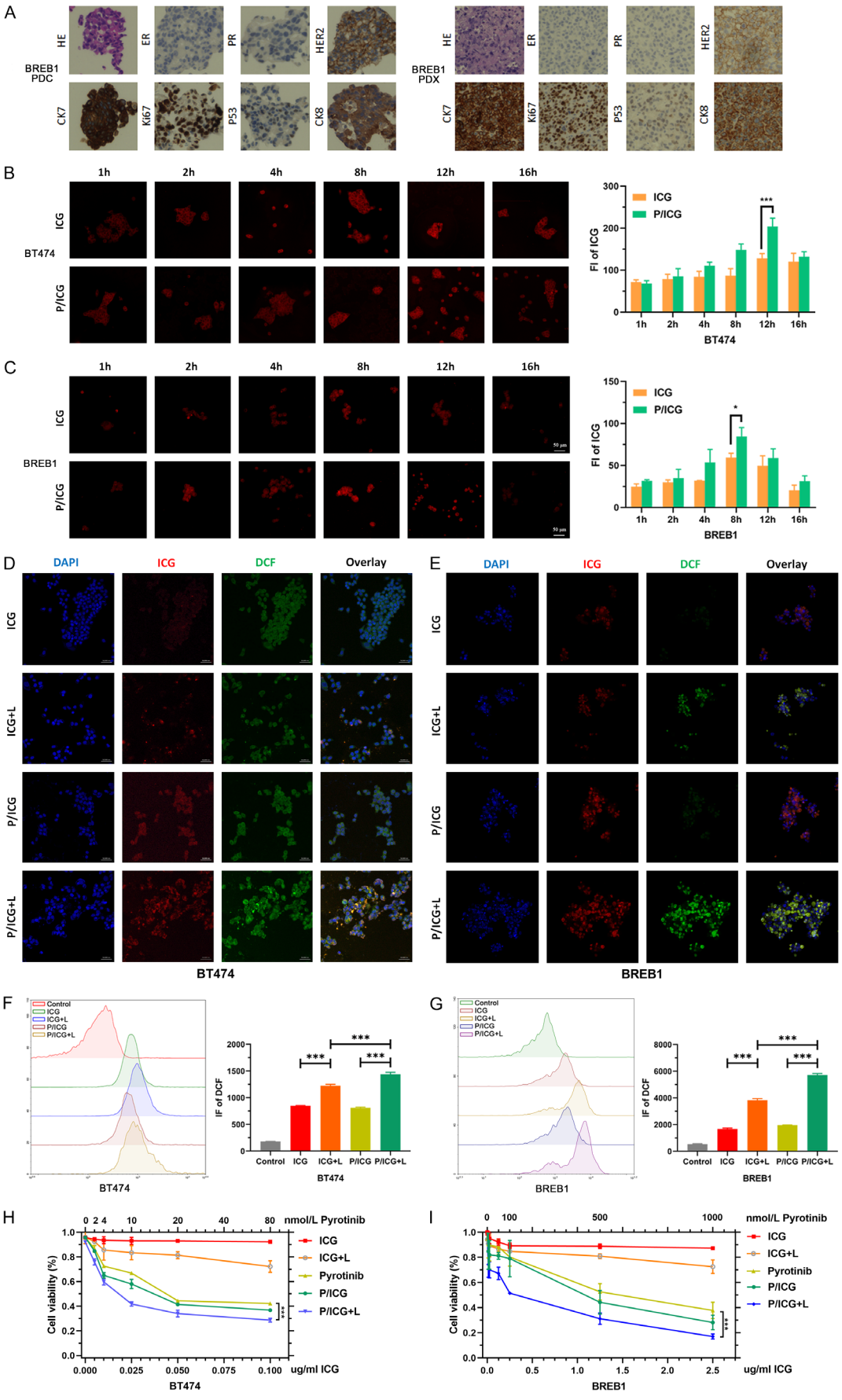
A
BREB1 PDC
HE
ER
PR
HER2
CK7
Ki67
P53
CK8
BREB1 PDX
B
1h
2h
4h
8h
12h
16h
ICG
P/ICG
BT474
FI of ICG
***
BT474
C
BREB1
*
BREB1
D
DAPI
ICG
DCF
Overlay
ICG+L
P/ICG
P/ICG+L
BT474
E
BREB1
F
Control
ICG
ICG+L
P/ICG
P/ICG+L
IF of DCF
BT474
G
BREB1
H
nmol/L Pyrotinib
0 2 4 10 20 40 80
Cell viability (%)
ICG
ICG+L
Pyrotinib
P/ICG
P/ICG+L
ug/ml ICG
BT474
I
0 100 500 1000
BREB1

Figure 4. Cellular uptake, photodynamics, and cellular toxicity of P/ICG in BT474 cells and BREB1 cells. A. H&E staining and immunohistochemistry of BREB1 cells and BREB1 cell-derived tissue. B, C. Confocal laser scanning microscopy and flow cytometry of cellular uptake of P/ICG at different time points in BT474 cells and BREB1 cells *in vitro*. D, E. Confocal laser scanning microscopy showing intracellular distribution and ROS production of P/ICG in BT474 cells and BREB1 cells *in vitro*. F, G. Flow cytometry showing ROS production of P/ICG in BT474 cells and BREB1 cells *in vitro*. H, I. Cytotoxicity assay of BT474 cells and BREB1 cells treated with free ICG, pyrotinib, or P/ICG, following 808-nm near-infrared light radiation for 5 min at a power density of 1.0 W/cm^2. Scale bar = 50 μm. **P* < 0.05, ***P* < 0.01, ****P* < 0.001.

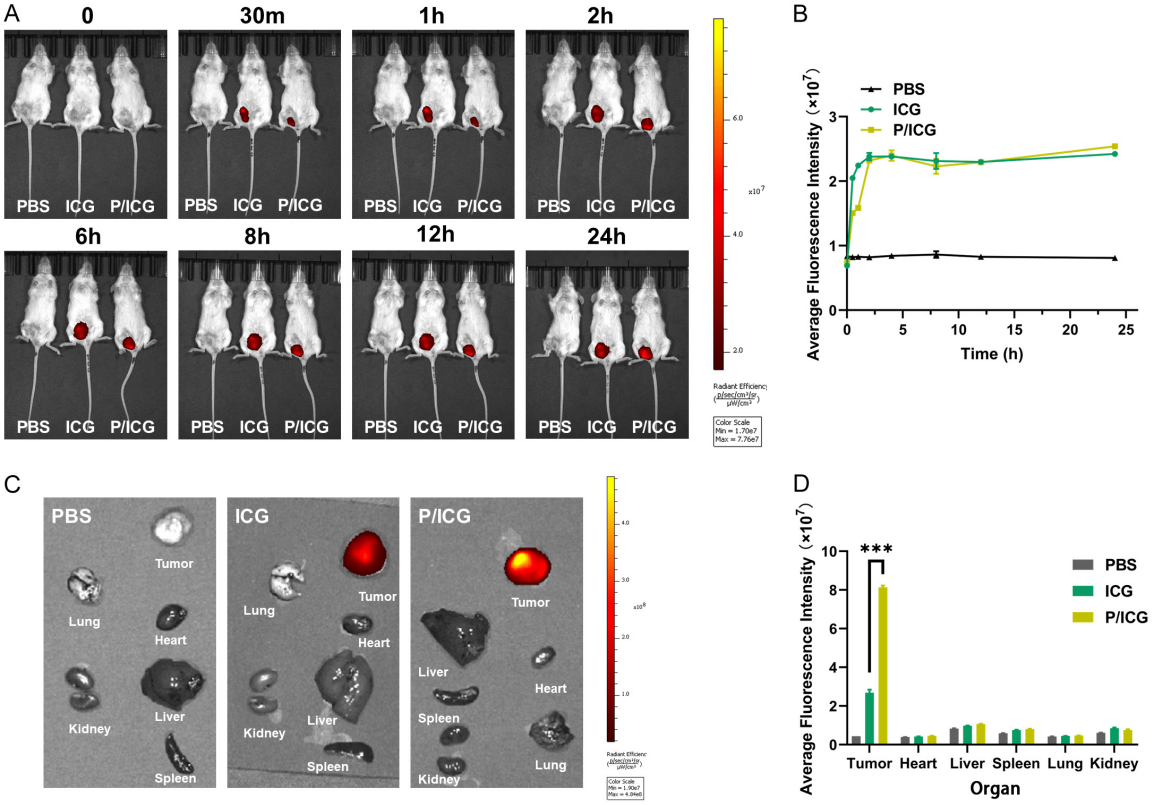

Figure 5. Fluorescence imaging and biodistribution of P/ICG *in vivo*. (A) Fluorescence imaging and (B) semiquantitative analyses of fluorescence intensity of P/ICG distribution in BREB1 tumor-bearing mice *in vivo* (n = 3, mean ± SD). (C) *Ex vivo* images and (D) and quantitative fluorescence analyses of uptake of PBS, free ICG, and P/ICG in the tumor, heart, lungs, liver, kidneys, and spleen 24 h after injection. ****P* < 0.001.

at a dosage of 0.5 mg/kg bodyweight, while the same volume of PBS was injected to mice in the control group. Two hours post-injection, the mice received 808-nm NIRL irradiation at a power density of 1.0 W/cm^2 for 5 minutes and the temperature was measured simultaneously with an infrared thermal imager (**Figure 6B**). The mean temperature of the tumor injected with P/ICG increased by 22.02°C within 2 minutes, whereas that of the tumor injected with free ICG increased by 18.44°C (**Figure 6C**).

The anti-tumor efficacy of PTT or PDT was monitored by measuring tumor volume and weight, alongside measuring the vital signs of mice every 2 days. A significant difference in the bodyweight of mice in each group was documented (**Figure 6D**). While no notable difference was observed between the control, ICG, and P/ICG groups in terms of tumor volume changes, both the P/ICG + L group and ICG + L group exhibited significant tumor reduction (ICG + L *vs*. control, *P* = 0.0416; P/ICG + L *vs*. control, *P* < 0.0001), with the P/ICG + L group showing greater reduction than the ICG + L group (P/ICG + L *vs*. ICG + L, *P* = 0.024) (**Figure 6E**).

Mice were euthanized, and their organs (such as heart, liver, spleen, lungs, and kidneys) and tumor tissues were harvested on day 14 for further analysis. The tumors in the ICG + L group

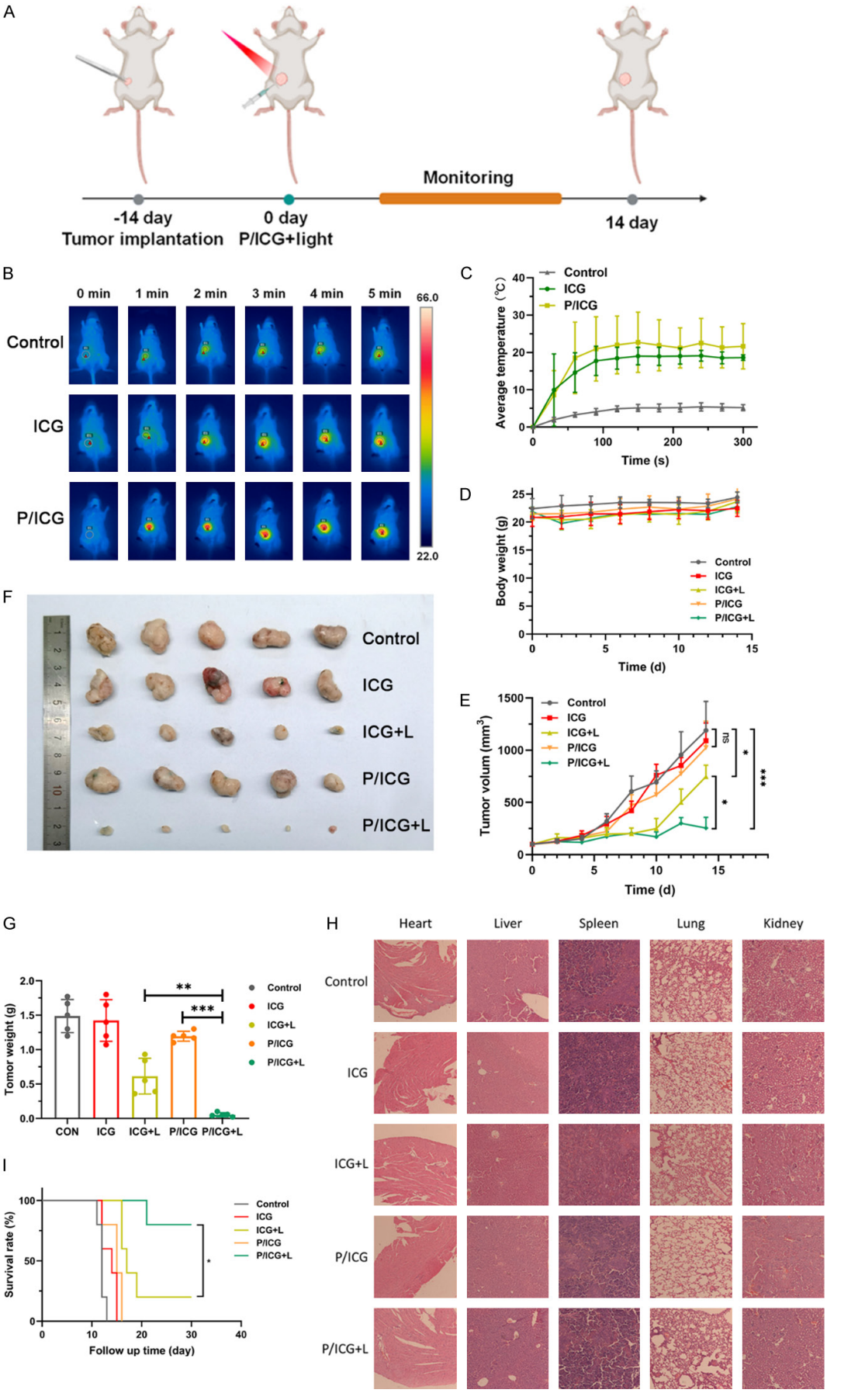
A
Monitoring
-14 day
Tumor implantation
0 day
P/ICG+light
14 day
B
0 min
1 min
2 min
3 min
4 min
5 min
66.0
22.0
Control
ICG
P/ICG
C
Control
ICG
P/ICG
Average temperature (℃)
Time (s)
D
Control
ICG
ICG+L
P/ICG
P/ICG+L
Body weight (g)
Time (d)
E
Control
ICG
ICG+L
P/ICG
P/ICG+L
Tumor volum (mm3)
Time (d)
ns
*
*
***
F
Control
ICG
ICG+L
P/ICG
P/ICG+L
G
Tomor weight (g)
**
***
CON
ICG
ICG+L
P/ICG
P/ICG+L
I
Survival rate (%)
Follow up time (day)
H
Heart
Liver
Spleen
Lung
Kidney
Control
ICG
ICG+L
P/ICG
P/ICG+L

Figure 6. Antitumor effect of P/ICG *in vivo*. (A) Flowchart showing establishment of a BREB1 cell-derived tumor model in mice and photothermal therapy and photodynamic treatment using P/ICG. (B) Infrared thermal images and (C) semiquantitative analyses of BREB1 tumor-bearing mice who received 808-nm near-infrared light radiation at a power density of 1.0 W/cm^2 at different time points (n = 5, mean ± SD). (D) Plot of tumor weight *versus* time of different groups. (E) Mean changes in tumor volume in different groups at different time points. (F) Tumor photographs taken from different groups of mice at day 14. (G) Tumor weight harvested from mice of different groups. (I) Survival curve of mice in different groups. (H) H&E sections of the heart, liver, spleen, lungs, and kidneys of mice in different groups at day 14. **P* < 0.05, ***P* < 0.01, ****P* < 0.001.

shrank to a certain extent, whereas the tumors in the P/ICG + L group showed significantly more pronounced shrinkage (*P* = 0.0018) (**Figure 6F** and **6G**). The average tumor weight in the P/ICG + L group was significantly lower than that in the ICG + L group (0.054 ± 0.02966 g vs. 1.390 ± 0.3578 g, *P* = 0.0018). Histological examination of organ sections stained with hematoxylin and eosin (H&E) showed no significant difference among groups (**Figure 6H**), suggesting that P/ICG treatment did not cause noticeable damage to the organs.

Survival rates were also assessed in another identical set of treatment groups (**Figure 6I**). Four weeks after drug injection, 80% of mice in the P/ICG + L group survived, significantly outperforming the other groups, indicating that P/ICG combined with NIRL irradiation markedly improved compared to free ICG with NIRL (*P* = 0.0316).

Therapeutic mechanisms of P/ICG for tumor suppression according to RNA-sequencing analysis

RNA-sequencing was conducted to explore the therapeutic mechanisms of P/ICG. Principal component analysis demonstrated genetic diversity among the P/ICG + L, P/ICG, and control groups (**Figure 7A**). Volcano plots highlighted the differences between the P/ICG + L and control group, as well as between P/ICG and the control group (**Figure 7B**). We identified 3,551 differentially expressed genes (DEGs) between the P/ICG group and control group: 2,432 genes were significantly upregulated, and 1,119 genes were downregulated. Additionally, 3,130 DEGs were observed between the P/ICG + L and control group: 2,089 genes were upregulated and 1,041 were downregulated.

Analyses of signaling pathways using the Kyoto Encyclopedia of Genes and Genomes (KEGG) database indicated that DEGs between the P/ICG + L and control group were primarily involved in processes like DNA replication, cell cycle, systemic lupus erythematosus, pathways in cancer, neutrophil extracellular trap formation, mismatch repair, and homologous recombination (**Figure 7C**). Notably, apoptosis was downregulated in the P/ICG group but upregulated in the P/ICG + L group, suggesting that reduced apoptosis may be a resistance mechanism in drugs targeting HER2-positive BC, which could be reversed by P/ICG treatment (Figure S2A). Further classification of enriched DEGs using the Search Tool for the Retrieval of Interacting Genes/Proteins (STRING) database identified 10 key pathways including inner dynein arm assembly, cilium movement involved in cell motility, axoneme assembly, positive regulation of apoptotic cell clearance, cellular response to biotic stimulus, cellular hormone metabolic process, cilium movement, response to lipopolysaccharide, hormone metabolic process, and cilium or flagellum-dependent cell motility (Figure S2B). Compared with the control group, P/ICG combined with NIRL irradiation inhibited pathways such as DNA replication, cell cycle, mismatch repair, homologous recombination, and the Cushing syndrome pathway. Conversely, it promoted pathways related to systemic lupus erythematosus, neutrophil extracellular trap formation, alcoholism, rheumatoid arthritis, and cytokine-cytokine receptor interaction pathway (Figure S2C and S2D). Overall, in the P/ICG + L group, the dominant pathways associated with DNA replication and repair, cell growth and death, immune system processes, and signal transduction (Table S1). Specifically, the pathways of cell growth and death, such as cell cycle, cellular senescence, apoptosis, p53 signaling pathway, oocyte meiosis, and ferroptosis, were significantly influenced by P/ICG.

Besides apoptosis, we considered ferroptosis as another potential anti-tumor mechanism for P/ICG, influenced by changes in the balance between ROS and glutathione due to photody-

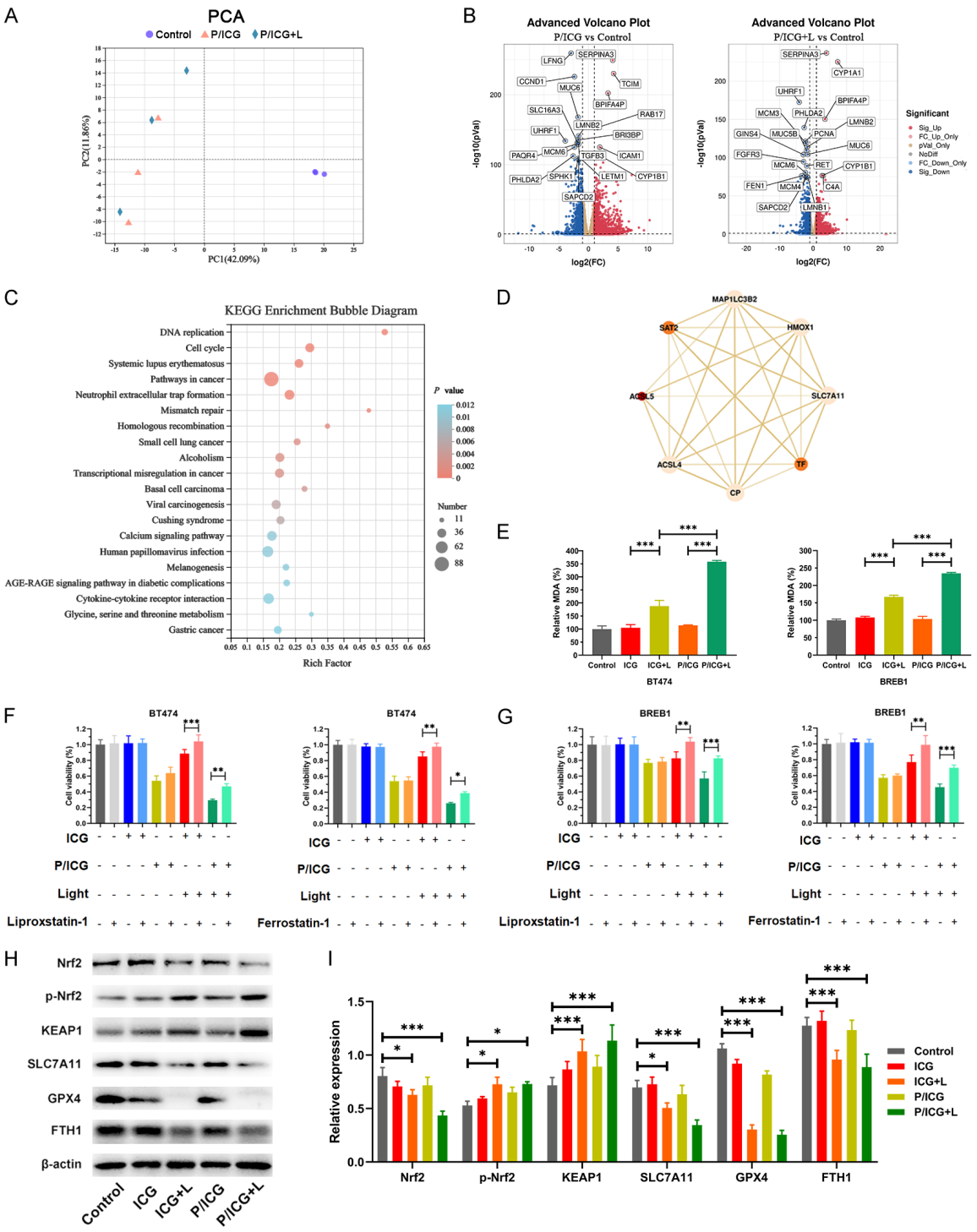

Figure 7. Therapeutic mechanisms of P/ICG for tumor suppression based on proteomics analysis. (A) PCA showing data gap between the P/ICG + L group and control group. (B) Volcano plot showing DEGs between the P/ICG + L group and control group. (C) Diagram showing DEGs between the P/ICG + L group and control group using the KEGG database focused mainly on "DNA replication", "cell cycle", "systemic lupus erythematosus", "pathways in cancer", "neutrophil extracellular trap formation", "mismatch repair", and "homologous recombination". (D) Correlation network diagram of eight hub DEGs related to ferroptosis. (E) Relative MDA level in BT474 cells and BREB1 cells in different groups. (F, G) Viability of BT474 cells and BREB1 cells treated with liproxstatin-1 or ferrostatin-1 in different groups. (H, I) Western blots showing expression of ferroptosis-related proteins in BREB1 cells administered different treatments. $^{*}P < 0.05$, $^{**}P < 0.01$, $^{***}P < 0.001$.

namic therapy (PDT). Eight hub genes associated with ferroptosis were notably affected by P/ICG, including TF, HMOX1, MAP1LC3B2, SAT2, CP, ACSL4, ACSL5, SLC7A11 (**Figure 7D**). Ferroptosis is an intracellular iron-dependent form of cell death, which is distinct from apoptosis, necrosis, and autophagy. Ferroptosis features prominently in tumor suppression and tumor immunity [42]. Initially, we quantified lipid peroxidation of BT474 and BREB1 cells by measuring the malondialdehyde (MDA) levels. MDA levels significantly increased after NIRL irradiation in both the P/ICG + L group and ICG + L group compared to their non-irradiated counterparts with marked differences noted (BT474 cells: P/ICG + L *vs*. ICG + L, $P < 0.0001$; P/ICG + L *vs*. P/ICG, $P < 0.0001$; BREB1 cells: P/ICG + L *vs*. ICG + L, $P < 0.0001$; P/ICG + L *vs*. P/ICG, $P < 0.0001$) (**Figure 7E**). Subsequently, we investigated the effects of the ferroptosis inhibitors on cell survival. Liproxstatin-1 (300 nM) and ferrostatin-1 (200 nM) were added to cell culture medium, respectively, followed by treatment with ICG or P/ICG. Twenty-four hours post-treatment, the cells were irradiated with NIRL, and cell survival was assessed using the Cell Counting Kit 8 (CCK8) Reagent. There was a significant increase in cell survival following NIR irradiation, highlighting that both PTT and PDT may actively promote ferroptosis (**Figure 7F** and **7G**).

To determine the involvement of PTT or PDT in ferroptosis, we analyzed the expression of ferroptosis-related proteins in BREB1 cells. Western blotting revealed that PTT and PDT significantly promoted the phosphorylation of nuclear factor erythroid 2-related factor 2 (Nrf2), upregulated the expression of free Kelch-like ECH-associated protein 1 (KEAP1), and simultaneously reduced the expression of SLC7A11, glutathione peroxidase 4 (GPX4), and ferritin heavy chain 1 (FTH1) (**Figure 7H** and **7I**). The Nrf2-KEAP1 signaling pathway, one of the important mechanisms of cell defense against oxidative-stress injury, participates in ferroptosis regulation. Proteins such as SLC7A11, GPX4, and FTH1 are involved in the reduction of glutathione and serve to inhibit ferroptosis [43-48]. These results indicate that PTT and PDT can activate the Nrf2-KEAP1 signaling pathway and suppress the expression of SLC7A11, GPX4, and FTH1. This modulation disturbs the balance between ROS and glutathione, enhances lipid peroxidation, and consequently promotes ferroptosis.

Discussion

Recently, nanomaterials have emerged as a promising alternative therapy for tumors, offering advantages such as non-invasive, minimally invasive, enhanced controllability, and lack of drug resistance [49]. Nanomaterials provide a new strategy for tumor immunotherapy, addressing a number of defects in conventional therapies, which often suffer from poor specificity, low immunogenicity, inadequate delivery efficiency, and off-target side effects [50]. Nanomaterials for tumor therapy utilized diverse basic biomaterials, including metal oxide, silicon, carbon nanotubes, polymer, natural bio-macromolecular, or cell-derived bioactive materials, serving as carriers for immunotherapeutic agents [51]. These materials enhance therapeutic efficacy by prolonging circulation time, optimizing pharmacokinetic parameters, ensuring target delivery, facilitating uptake and presentation, and control release. This multifaceted approach effectively compensates for the limitations traditionally associated with immunotherapy [52].

Traditional breast cancer treatment typically includes combinations of surgery, radiation, chemotherapy, hormone, and targeted therapy [53-56]. However, recent advances in nanotechnology offer new synergistic approaches for managing this disease. For instance, Qin et al. developed platelet membrane-camouflaged magnetic nanoparticles, Fe_3O_4-SAS @ PLT, aimed at treating triple-negative breast cancer. The experiment revealed that Fe_3O_4-SAS @ PLT-mediated ferroptosis not only enhances tumor-specific immune response but also effectively reprograms immunosuppressive M2 macrophages into antitumor M1 subtype [57]. Furthermore, the HA-b-PCDA polymeric nanomaterial platform was designed to simultaneously deliver chemotherapeutic drugs and target breast cancer stem cells, significantly inhibiting the proliferation and stemness of breast cancer stem cell-enriched 4T1 mammospheres [58]. In another innovative approach, Hao et al. developed nanoparticles composed of doxorubicin, chitosan, and cell-penetrating peptide, loaded with ginsenoside Rg3. These nanoparticles are designed to reverse the immunosuppressive tumor micro-

environment and promote immunogenic cell death in 4T1 tumors [59]. Moreover, according to the research by Zhuofei et al., a new biodegradable polymeric nanoparticle platform encapsuling RNA1 has been shown to reverse radio-resistance of triple-negative breast cancer by inducing long noncoding RNA AFAP1-AS1 silencing and restraining Wnt/β-Catenin signaling pathway [60].

In recent years, nano-biomaterials for tumor PTT and PDT stimulated by NIRL have garnered significant attention. Near infrared light, which includes two primary regions, 650-950 nm and 1,000-1,350 nm, offers minimal absorption by water and biomolecules, allowing it to penetrate deep tissues without significant damage to normal tissues. This attribute makes NIRL particularly effective for therapeutic applications in deep-seated tumors. PTT and PDT offer high selectivity and specificity, and they can be conveniently integrated with other therapeutic regimen such as chemotherapy, radiation therapy, immunotherapy or gene therapy [61]. By targeting photosensitizers to specific cells, not only can the photothermal efficiency be improved, but also damage to surrounding normal tissues can be minimized. This targeted approach allows for a multi-mode synergistic anti-tumor effect that encompasses cell death, cell immunity, and modulation of extracellular matrix [62].

In summary, this research introduces innovative targeted photothermal nanomaterials by combining a HER2-targeted drug with indocyanine green. These materials are designed to precisely target tumor cells, delivering an accurate and potent anti-tumor effect.

Conclusions

We developed a new nanodrug, P/ICG, which combines pyrotinib and ICG for targeted and multimodal synergistic therapy of drug-resistant HER2-positive BC. P/ICG integrated the advantages of pyrotinib and ICG: pyrotinib enhances the targeting of nanomaterials to tumor cells, while the photothermal and photodynamic properties of ICG amplify the chemotherapeutic effects of pyrotinib, resulting in a stronger anticancer effect. Intratumor injection is utilized to overcome the interstitial barrier associated with the tumor, allowing for precise and uniform drug distribution directly to the tumor site and ensuring a sustained therapeutic effect. P/ICG exerts its photothermal and photodynamic effects by increasing ROS and elevating intracellular temperature. The equilibrium shift of ROS and glutathione, along with the downregulation of ferroptosis-related protective proteins due to high temperature, enhances lipid peroxidation and promotes ferroptosis. The present nanodrug holds three main advantages: (1) pyrotinib provides effective targeting of HER2; (2) the combined anticancer activity of pyrotinib and the photothermal and photodynamic effects of ICG result in a highly potent anti-cancer effect; (3) local injection and NIRL irradiation enable precise *in situ* ablation of tumor cells with minimal damage to surrounding normal tissues.

Our research provides a novel integrated approach against HER2-positive BC, employing a targeted and multimodal synergistic strategy.

Acknowledgements

This study was supported by Chongqing Outstanding Youth Natural Science Fund (CSTB2023NSCQ-JQX0012), and Chongqing Key Projects of Technological Innovation and Application Development (CSTB2022TIAD-KPX0168).

Disclosure of conflict of interest

None.

Address correspondence to: Xiaowei Qi and Jun Jiang, Department of Breast and Thyroid Surgery, Southwest Hospital, Army Medical University, Chongqing 400038, China. E-mail: qxw9908@foxmail.com (XWQ); jcbd@medmail.com.cn (JJ); Jing Zhang, Department of Laboratory Medicine, Nanfang Hospital, Southern Medical University, Guangzhou 510515, Guangdong, China. E-mail: zhangjingzisefeng@163.com

References

[1] Siegel RL, Miller KD, Wagle NS and Jemal A. Cancer statistics, 2023. CA Cancer J Clin 2023; 73: 17-48.

[2] Qiu H, Cao S and Xu R. Cancer incidence, mortality, and burden in China: a time-trend analysis and comparison with the United States and United Kingdom based on the global epidemiological data released in 2020. Cancer Commun (Lond) 2021; 41: 1037-1048.

[3] Liu N, Yang DW, Wu YX, Xue WQ, Li DH, Zhang JB, He YQ and Jia WH. Burden, trends, and risk factors for breast cancer in China from 1990 to 2019 and its predictions until 2034: an up-to-date overview and comparison with those in Japan and South Korea. BMC Cancer 2022; 22: 826.

[4] Jiang YZ, Ma D, Jin X, Xiao Y, Yu Y, Shi J, Zhou YF, Fu T, Lin CJ, Dai LJ, Liu CL, Zhao S, Su GH, Hou W, Liu Y, Chen Q, Yang J, Zhang N, Zhang WJ, Liu W, Ge W, Yang WT, You C, Gu Y, Kaklamani V, Bertucci F, Verschraegen C, Daemen A, Shah NM, Wang T, Guo T, Shi L, Perou CM, Zheng Y, Huang W and Shao ZM. Integrated multiomic profiling of breast cancer in the Chinese population reveals patient stratification and therapeutic vulnerabilities. Nat Cancer 2024; 5: 673-690.

[5] Wolff AC, Hammond ME, Hicks DG, Dowsett M, McShane LM, Allison KH, Allred DC, Bartlett JM, Bilous M, Fitzgibbons P, Hanna W, Jenkins RB, Mangu PB, Paik S, Perez EA, Press MF, Spears PA, Vance GH, Viale G and Hayes DF; American Society of Clinical Oncology; College of American Pathologists. Recommendations for human epidermal growth factor receptor 2 testing in breast cancer: American Society of Clinical Oncology/College of American Pathologists clinical practice guideline update. J Clin Oncol 2013; 31: 3997-4013.

[6] Piccart-Gebhart MJ, Procter M, Leyland-Jones B, Goldhirsch A, Untch M, Smith I, Gianni L, Baselga J, Bell R, Jackisch C, Cameron D, Dowsett M, Barrios CH, Steger G, Huang CS, Andersson M, Inbar M, Lichinitser M, Lang I, Nitz U, Iwata H, Thomssen C, Lohrisch C, Suter TM, Ruschoff J, Suto T, Greatorex V, Ward C, Straehle C, McFadden E, Dolci MS and Gelber RD; Herceptin Adjuvant (HERA) Trial Study Team. Trastuzumab after adjuvant chemotherapy in HER2-positive breast cancer. N Engl J Med 2005; 353: 1659-1672.

[7] Menard S, Tagliabue E, Campiglio M and Pupa SM. Role of HER2 gene overexpression in breast carcinoma. J Cell Physiol 2000; 182: 150-162.

[8] Slamon DJ, Leyland-Jones B, Shak S, Fuchs H, Paton V, Bajamonde A, Fleming T, Eiermann W, Wolter J, Pegram M, Baselga J and Norton L. Use of chemotherapy plus a monoclonal antibody against HER2 for metastatic breast cancer that overexpresses HER2. N Engl J Med 2001; 344: 783-792.

[9] Roth J, Bajaj P, Sullivan S, Reyes C, Antao V, Stein A and Mahtani R. 263PSurvival gains from advances in first-line systemic therapy for HER2-positive metastatic breast cancer in the U.S., 1995-2015. Ann Oncol 2017; 28.

[10] Hudis CA. Trastuzumab--mechanism of action and use in clinical practice. N Engl J Med 2007; 357: 39-51.

[11] Veeraraghavan J, De Angelis C, Reis-Filho JS, Pascual T, Prat A, Rimawi MF, Osborne CK and Schiff R. De-escalation of treatment in HER2-positive breast cancer: determinants of response and mechanisms of resistance. Breast 2017; 34 Suppl 1: S19-S26.

[12] Goutsouliak K, Veeraraghavan J, Sethunath V, De Angelis C, Osborne CK, Rimawi MF and Schiff R. Towards personalized treatment for early stage HER2-positive breast cancer. Nat Rev Clin Oncol 2020; 17: 233-250.

[13] Gianni L, Pienkowski T, Im YH, Roman L, Tseng LM, Liu MC, Lluch A, Staroslawska E, de la Haba-Rodriguez J, Im SA, Pedrini JL, Poirier B, Morandi P, Semiglazov V, Srimuninnimit V, Bianchi G, Szado T, Ratnayake J, Ross G and Valagussa P. Efficacy and safety of neoadjuvant pertuzumab and trastuzumab in women with locally advanced, inflammatory, or early HER2-positive breast cancer (NeoSphere): a randomised multicentre, open-label, phase 2 trial. Lancet Oncol 2012; 13: 25-32.

[14] Baselga J, Bradbury I, Eidtmann H, Di Cosimo S, de Azambuja E, Aura C, Gómez H, Dinh P, Fauria K, Van Dooren V, Aktan G, Goldhirsch A, Chang TW, Horváth Z, Coccia-Portugal M, Domont J, Tseng LM, Kunz G, Sohn JH, Semiglazov V, Lerzo G, Palacova M, Probachai V, Pusztai L, Untch M, Gelber RD and Piccart-Gebhart M; NeoALTTO Study Team. Lapatinib with trastuzumab for HER2-positive early breast cancer (NeoALTTO): a randomised, open-label, multicentre, phase 3 trial. Lancet 2012; 379: 633-640.

[15] Hurvitz SA, Martin M, Symmans WF, Jung KH, Huang CS, Thompson AM, Harbeck N, Valero V, Stroyakovskiy D, Wildiers H, Campone M, Boileau JF, Beckmann MW, Afenjar K, Fresco R, Helms HJ, Xu J, Lin YG, Sparano J and Slamon D. Neoadjuvant trastuzumab, pertuzumab, and chemotherapy versus trastuzumab emtansine plus pertuzumab in patients with HER2-positive breast cancer (KRISTINE): a randomised, open-label, multicentre, phase 3 trial. Lancet Oncol 2018; 19: 115-126.

[16] Gianni L, Pienkowski T, Im YH, Tseng LM, Liu MC, Lluch A, Starosławska E, de la Haba-Rodriguez J, Im SA, Pedrini JL, Poirier B, Morandi P, Semiglazov V, Srimuninnimit V, Bianchi GV, Magazzù D, McNally V, Douthwaite H, Ross G and Valagussa P. 5-year analysis of neoadjuvant pertuzumab and trastuzumab in patients with locally advanced, inflammatory, or early-stage HER2-positive breast cancer (NeoSphere): a multicentre, open-label, phase 2

randomised trial. Lancet Oncol 2016; 17: 791-800.
[17] Gianni L, Eiermann W, Semiglazov V, Manikhas A, Lluch A, Tjulandin S, Zambetti M, Vazquez F, Byakhow M, Lichinitser M, Climent MA, Ciruelos E, Ojeda B, Mansutti M, Bozhok A, Baronio R, Feyereislova A, Barton C, Valagussa P and Baselga J. Neoadjuvant chemotherapy with trastuzumab followed by adjuvant trastuzumab versus neoadjuvant chemotherapy alone, in patients with HER2-positive locally advanced breast cancer (the NOAH trial): a randomised controlled superiority trial with a parallel HER2-negative cohort. Lancet 2010; 375: 377-384.
[18] de Azambuja E, Holmes AP, Piccart-Gebhart M, Holmes E, Di Cosimo S, Swaby RF, Untch M, Jackisch C, Lang I, Smith I, Boyle F, Xu B, Barrios CH, Perez EA, Azim HA Jr, Kim SB, Kuemmel S, Huang CS, Vuylsteke P, Hsieh RK, Gorbunova V, Eniu A, Dreosti L, Tavartkiladze N, Gelber RD, Eidtmann H and Baselga J. Lapatinib with trastuzumab for HER2-positive early breast cancer (NeoALTTO): survival outcomes of a randomised, open-label, multicentre, phase 3 trial and their association with pathological complete response. Lancet Oncol 2014; 15: 1137-1146.
[19] Yu J, Javier D, Yaseen MA, Nitin N, Richards-Kortum R, Anvari B and Wong MS. Self-assembly synthesis, tumor cell targeting, and photothermal capabilities of antibody-coated indocyanine green nanocapsules. J Am Chem Soc 2010; 132: 1929-1938.
[20] Li S, Zhang W, Xing R, Yuan C, Xue H and Yan X. Supramolecular nanofibrils formed by coassembly of clinically approved drugs for tumor photothermal immunotherapy. Adv Mater 2021; 33: e2100595.
[21] Gobin AM, Lee MH, Halas NJ, James WD, Drezek RA and West JL. Near-infrared resonant nanoshells for combined optical imaging and photothermal cancer therapy. Nano Lett 2007; 7: 1929-1934.
[22] Weissleder R. A clearer vision for in vivo imaging. Nat Biotechnol 2001; 19: 316-317.
[23] Jin Y, Yuan L, Zhang Y, Tang P, Yang Y, Fan L, Chen L, Qi X and Jiang J. A prospective self-controlled study of indocyanine green, radioisotope, and methylene blue for combined imaging of axillary sentinel lymph nodes in breast cancer. Front Oncol 2022; 12: 803804.
[24] Ntziachristos V, Yodh AG, Schnall M and Chance B. Concurrent MRI and diffuse optical tomography of breast after indocyanine green enhancement. Proc Natl Acad Sci U S A 2000; 97: 2767-2772.
[25] Hutteman M, Mieog JS, van der Vorst JR, Liefers GJ, Putter H, Löwik CW, Frangioni JV, van de Velde CJ and Vahrmeijer AL. Randomized, double-blind comparison of indocyanine green with or without albumin premixing for near-infrared fluorescence imaging of sentinel lymph nodes in breast cancer patients. Breast Cancer Res Treat 2011; 127: 163-170.
[26] Schaafsma BE, Mieog JS, Hutteman M, van der Vorst JR, Kuppen PJ, Löwik CW, Frangioni JV, van de Velde CJ and Vahrmeijer AL. The clinical use of indocyanine green as a near-infrared fluorescent contrast agent for image-guided oncologic surgery. J Surg Oncol 2011; 104: 323-332.
[27] Feng B, Niu Z, Hou B, Zhou L, Li Y and Yu H. Enhancing triple negative breast cancer immunotherapy by ICG-templated self-assembly of paclitaxel nanoparticles. Adv Funct Mater 2019; 30: 1906605.
[28] Zou Y, Li M, Xiong T, Zhao X, Du J, Fan J and Peng X. A single molecule drug targeting photosensitizer for enhanced breast cancer photothermal therapy. Small 2020; 16: e1907677.
[29] Zhu Y, Li L, Zhang G, Wan H, Yang C, Diao X, Chen X, Zhang L and Zhong D. Metabolic characterization of pyrotinib in humans by ultra-performance liquid chromatography/quadrupole time-of-flight mass spectrometry. J Chromatogr B Analyt Technol Biomed Life Sci 2016; 1033-1034: 117-127.
[30] Ma F, Li Q, Chen S, Zhu W, Fan Y, Wang J, Luo Y, Xing P, Lan B, Li M, Yi Z, Cai R, Yuan P, Zhang P, Li Q and Xu B. Phase I study and biomarker analysis of pyrotinib, a novel irreversible pan-ErbB receptor tyrosine kinase inhibitor, in patients with human epidermal growth factor receptor 2-positive metastatic breast cancer. J Clin Oncol 2017; 35: 3105-3112.
[31] Meng J, Liu XY, Ma S, Zhang H, Yu SD, Zhang YF, Chen MX, Zhu XY, Liu Y, Yi L, Ding XL, Chen XY, Miao LY and Zhong DF. Metabolism and disposition of pyrotinib in healthy male volunteers: covalent binding with human plasma protein. Acta Pharmacol Sin 2019; 40: 980-988.
[32] Xuhong JC, Qi XW, Zhang Y and Jiang J. Mechanism, safety and efficacy of three tyrosine kinase inhibitors lapatinib, neratinib and pyrotinib in HER2-positive breast cancer. Am J Cancer Res 2019; 9: 2103-2119.
[33] Ma F, Ouyang Q, Li W, Jiang Z, Tong Z, Liu Y, Li H, Yu S, Feng J, Wang S, Hu X, Zou J, Zhu X and Xu B. Pyrotinib or lapatinib combined with capecitabine in HER2-positive metastatic breast cancer with prior taxanes, anthracyclines, and/or trastuzumab: a randomized, phase II study. J Clin Oncol 2019; 37: 2610-2619.
[34] Jiang Z, Yan M, Hu X, Zhang Q, Ouyang Q, Feng J, Yin Y, Sun T, Tong Z, Wang X, Yao H, Zou J and Zhu X. Pyrotinib combined with capecitabine in

women with HER2+ metastatic breast cancer previously treated with trastuzumab and taxanes: a randomized phase III study. J Clin Oncol 2019; 37: 1001.
[35] Xuhong J, Qi X, Tang P, Fan L, Chen L, Zhang F, Tan X, Yan W, Zhong L, He C, Liang Y, Ren L, Wang M, Zhang Y and Jiang J. Neoadjuvant pyrotinib plus trastuzumab and chemotherapy for stage I-III HER2-positive breast cancer: a phase II clinical trial. Oncologist 2020; 25: e1909-e1920.
[36] Yan M, Bian L, Hu X, Zhang Q, Ouyang Q, Feng J, Yin Y, Sun T, Tong Z, Wang X, Yao H, Zou J, Zhu X and Jiang Z. Pyrotinib plus capecitabine for human epidermal growth factor receptor 2-positive metastatic breast cancer after trastuzumab and taxanes (PHENIX): a randomized, double-blind, placebo-controlled phase 3 study. Transl Breast Cancer Res 2020; 1: 13.
[37] Xu B, Yan M, Ma F, Hu X, Feng J, Ouyang Q, Tong Z, Li H, Zhang Q, Sun T, Wang X, Yin Y, Cheng Y, Li W, Gu Y, Chen Q, Liu J, Cheng J, Geng C, Qin S, Wang S, Lu J, Shen K, Liu Q, Wang X, Wang H, Luo T, Yang J, Wu Y, Yu Z, Zhu X, Chen C and Zou J; PHOEBE Investigators. Pyrotinib plus capecitabine versus lapatinib plus capecitabine for the treatment of HER2-positive metastatic breast cancer (PHOEBE): a multicentre, open-label, randomised, controlled, phase 3 trial. Lancet Oncol 2021; 22: 351-360.
[38] Wu J, Liu Z, Yang H, Tang J, Wang K, Liu Y, Wang H, Fu P, Zhang S, Liu Q, Jiang Z, Wang S, Huang J, Wang C, Wang S, Wang Y, Zhen L, Zhu X, Wu F, Zhang T and Zou J. Abstract PD8-08: pyrotinib in combination with trastuzumab and docetaxel as neoadjuvant treatment for HER2-positive early or locally advanced breast cancer (PHEDRA): a randomized, double-blind, multicenter, phase 3 study. Cancer Res 2022; 82: PD8-08.
[39] Xie S, Sun W, Zhang C, Dong B, Yang J, Hou M, Xiong L, Cai B, Liu X and Xue W. Metabolic control by heat stress determining cell fate to ferroptosis for effective cancer therapy. ACS Nano 2021; 15: 7179-7194.
[40] Friedmann Angeli JP, Schneider M, Proneth B, Tyurina YY, Tyurin VA, Hammond VJ, Herbach N, Aichler M, Walch A, Eggenhofer E, Basavarajappa D, Radmark O, Kobayashi S, Seibt T, Beck H, Neff F, Esposito I, Wanke R, Forster H, Yefremova O, Heinrichmeyer M, Bornkamm GW, Geissler EK, Thomas SB, Stockwell BR, O'Donnell VB, Kagan VE, Schick JA and Conrad M. Inactivation of the ferroptosis regulator Gpx4 triggers acute renal failure in mice. Nat Cell Biol 2014; 16: 1180-1191.
[41] Dixon SJ, Lemberg KM, Lamprecht MR, Skouta R, Zaitsev EM, Gleason CE, Patel DN, Bauer AJ, Cantley AM, Yang WS, Morrison B 3rd and Stockwell BR. Ferroptosis: an iron-dependent form of nonapoptotic cell death. Cell 2012; 149: 1060-1072.
[42] Lei G, Zhuang L and Gan B. Targeting ferroptosis as a vulnerability in cancer. Nat Rev Cancer 2022; 22: 381-396.
[43] Wang Z. Iron regulation in ferroptosis. Nat Cell Biol 2023; 25: 515.
[44] Dong H, Xia Y, Jin S, Xue C, Wang Y, Hu R and Jiang H. Nrf2 attenuates ferroptosis-mediated IIR-ALI by modulating TERT and SLC7A11. Cell Death Dis 2021; 12: 1027.
[45] Abdalkader M, Lampinen R, Kanninen KM, Malm TM and Liddell JR. Targeting Nrf2 to suppress ferroptosis and mitochondrial dysfunction in neurodegeneration. Front Neurosci 2018; 12: 466.
[46] Yan Y, Teng H, Hang Q, Kondiparthi L, Lei G, Horbath A, Liu X, Mao C, Wu S, Zhuang L, James You M, Poyurovsky MV, Ma L, Olszewski K and Gan B. SLC7A11 expression level dictates differential responses to oxidative stress in cancer cells. Nat Commun 2023; 14: 3673.
[47] Forcina GC and Dixon SJ. GPX4 at the crossroads of lipid homeostasis and ferroptosis. Proteomics 2019; 19: e1800311.
[48] Tang D, Chen X, Kang R and Kroemer G. Ferroptosis: molecular mechanisms and health implications. Cell Res 2021; 31: 107-125.
[49] Liu Y, Bhattarai P, Dai Z and Chen X. Photothermal therapy and photoacoustic imaging via nanotheranostics in fighting cancer. Chem Soc Rev 2019; 48: 2053-2108.
[50] Yan S, Luo Z, Li Z, Wang Y, Tao J, Gong C and Liu X. Improving cancer immunotherapy outcomes using biomaterials. Angew Chem Int Ed Engl 2020; 59: 17332-17343.
[51] Xiao M, Tang Q, Zeng S, Yang Q, Yang X, Tong X, Zhu G, Lei L and Li S. Emerging biomaterials for tumor immunotherapy. Biomater Res 2023; 27: 47.
[52] Ruan S, Huang Y, He M and Gao H. Advanced biomaterials for cell-specific modulation and restore of cancer immunotherapy. Adv Sci (Weinh) 2022; 9: e2200027.
[53] Zerella MA, Zaffaroni M, Ronci G, Dicuonzo S, Rojas DP, Morra A, Gerardi MA, Fodor C, Rondi E, Vigorito S, Penco S, Sargenti M, Baratella P, Vicini E, Morigi C, Kahler-Ribeiro-Fontana S, Galimberti VE, Gandini S, De Camilli E, Renne G, Cattani F, Veronesi P, Orecchia R, Jereczek-Fossa BA and Leonardi MC. A narrative review for radiation oncologists to implement preoperative partial breast irradiation. Radiol Med 2023; 128: 1553-1570.
[54] Wang HL, Ma X, Guan XY, Song C, Li GB, Yu YM and Yang LL. Potential synthetic lethality for breast cancer: a selective sirtuin 2 inhibitor

combined with a multiple kinase inhibitor sorafenib. Pharmacol Res 2022; 177: 106050.
[55] Meattini I, Palumbo I, Becherini C, Borghesi S, Cucciarelli F, Dicuonzo S, Fiorentino A, Spoto R, Poortmans P, Aristei C and Livi L. The Italian Association for Radiotherapy and Clinical Oncology (AIRO) position statements for postoperative breast cancer radiation therapy volume, dose, and fractionation. Radiol Med 2022; 127: 1407-1411.
[56] Korde LA, Somerfield MR, Carey LA, Crews JR, Denduluri N, Hwang ES, Khan SA, Loibl S, Morris EA, Perez A, Regan MM, Spears PA, Sudheendra PK, Symmans WF, Yung RL, Harvey BE and Hershman DL. Neoadjuvant chemotherapy, endocrine therapy, and targeted therapy for breast cancer: ASCO guideline. J Clin Oncol 2021; 39: 1485-1505.
[57] Jiang Q, Wang K, Zhang X, Ouyang B, Liu H, Pang Z and Yang W. Platelet membrane-camouflaged magnetic nanoparticles for ferroptosis-enhanced cancer immunotherapy. Small 2020; 16: e2001704.
[58] Lv L, Shi Y, Deng Z, Xu J, Ye Z, He J, Chen G, Yu X, Wu J, Huang X and Li G. A polymeric nanocarrier that eradicates breast cancer stem cells and delivers chemotherapeutic drugs. Biomater Res 2023; 27: 133.
[59] Wu H, Wei G, Luo L, Li L, Gao Y, Tan X, Wang S, Chang H, Liu Y, Wei Y, Song J, Zhang Z and Huo J. Ginsenoside Rg3 nanoparticles with permeation enhancing based chitosan derivatives were encapsulated with doxorubicin by thermosensitive hydrogel and anti-cancer evaluation of peritumoral hydrogel injection combined with PD-L1 antibody. Biomater Res 2022; 26: 77.
[60] Bi Z, Li Q, Dinglin X, Xu Y, You K, Hong H, Hu Q, Zhang W, Li C, Tan Y, Xie N, Ren W, Li C, Liu Y, Hu H, Xu X and Yao H. Nanoparticles (NPs)-meditated LncRNA AFAP1-AS1 silencing to block Wnt/β-catenin signaling pathway for synergistic reversal of radioresistance and effective cancer radiotherapy. Adv Sci (Weinh) 2020; 7: 2000915.
[61] Duan S, Hu Y, Zhao Y, Tang K, Zhang Z, Liu Z, Wang Y, Guo H, Miao Y, Du H, Yang D, Li S and Zhang J. Nanomaterials for photothermal cancer therapy. RSC Adv 2023; 13: 14443-14460.
[62] Overchuk M, Weersink RA, Wilson BC and Zheng G. Photodynamic and photothermal therapies: synergy opportunities for nanomedicine. ACS Nano 2023; 17: 7979-8003.

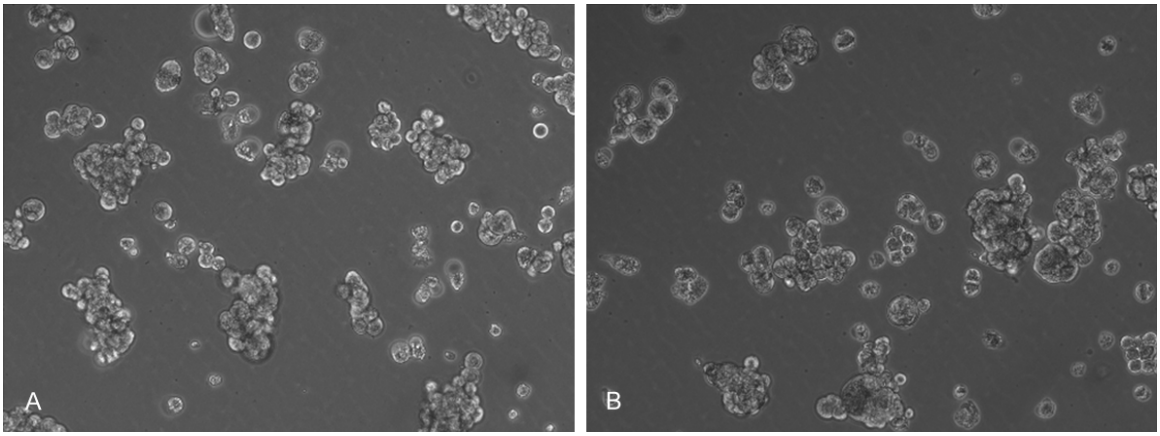

Figure S1. BREB1 cells are purified cancer cells that can grow in a suspension in a specific medium and proliferate stably.

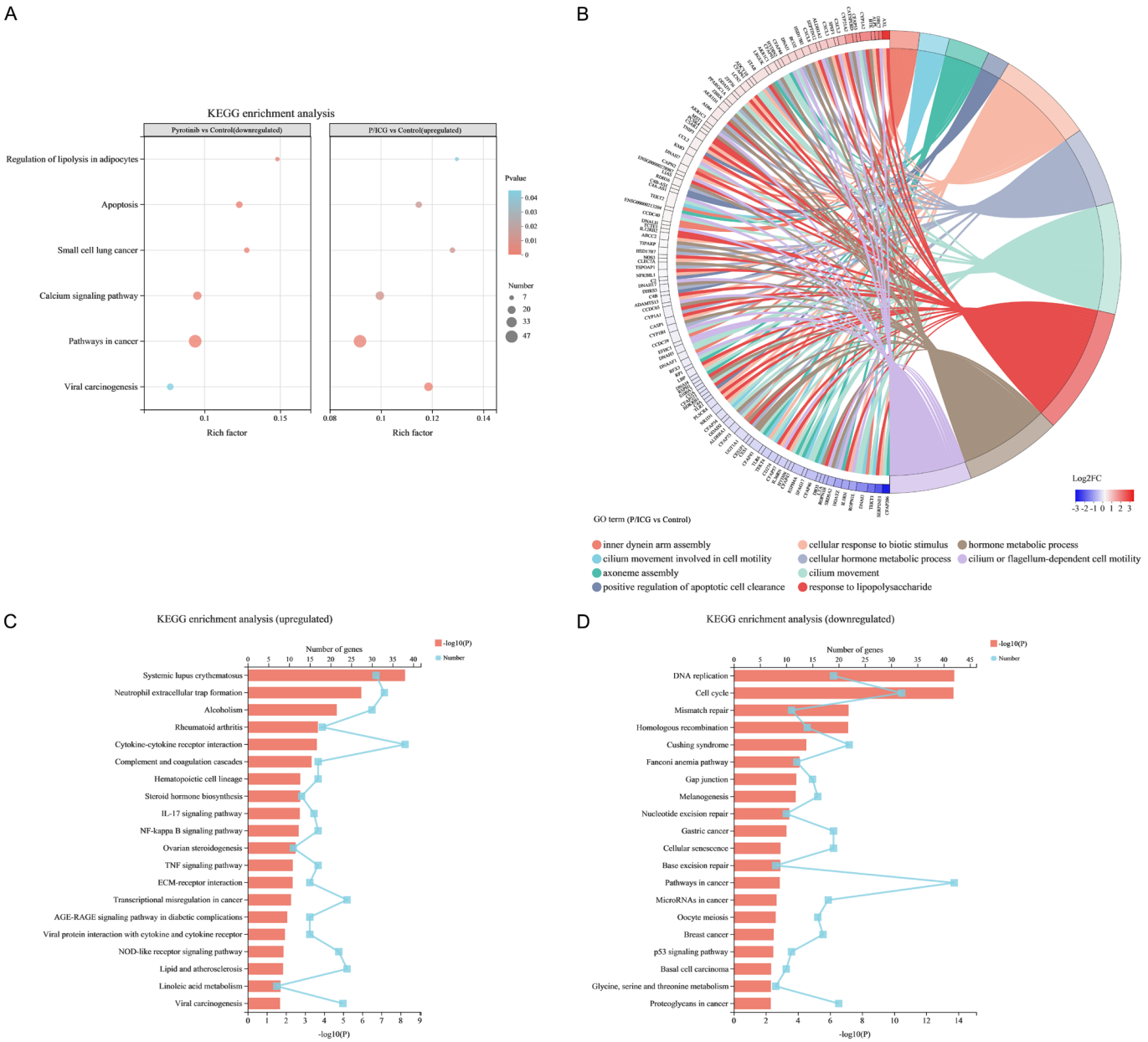

Figure S2. RNA-sequencing showing the therapeutic mechanism of P/ICG. A. Signaling-pathway enrichment using the KEGG database. B. Gene classification using the STRING database. C, D. KEGG enrichment analysis of upregulated and downregulated pathway.

Table S1. KEGG signaling pathways

Pathway id	Description	Ratio_in_study	Ratio_in_pop	*P* value	First Category	Second Category
hsa03030	DNA replication	19/1514	36/14529	2.96E-10	Genetic Information Processing	Replication and repair
hsa04110	Cell cycle	36/1514	122/14529	4.19E-09	Cellular Processes	Cell growth and death
hsa05322	Systemic lupus erythematosus	34/1514	130/14529	2.90E-07	Human Diseases	Immune disease
hsa05200	Pathways in cancer	88/1514	501/14529	5.47E-07	Human Diseases	Cancer: overview
hsa04613	Neutrophil extracellular trap formation	42/1514	181/14529	4.50E-07	Organismal Systems	Immune system
hsa03430	Mismatch repair	11/1514	23/14529	6.25E-06	Genetic Information Processing	Replication and repair
hsa03440	Homologous recombination	14/1514	40/14529	2.85E-05	Genetic Information Processing	Replication and repair
hsa05222	Small cell lung cancer	22/1514	86/14529	5.05E-05	Human Diseases	Cancer: specific types
hsa05034	Alcoholism	36/1514	178/14529	7.09E-05	Human Diseases	Substance dependence
hsa05202	Transcriptional misregulation in cancer	37/1514	184/14529	6.44E-05	Human Diseases	Cancer: overview
hsa05217	Basal cell carcinoma	17/1514	61/14529	0.000113394	Human Diseases	Cancer: specific types
hsa05203	Viral carcinogenesis	37/1514	194/14529	0.000200865	Human Diseases	Cancer: overview
hsa04934	Cushing syndrome	30/1514	147/14529	0.00023309	Human Diseases	Endocrine and metabolic disease
hsa04020	Calcium signaling pathway	41/1514	231/14529	0.000457937	Environmental Information Processing	Signal transduction
hsa05165	Human papillomavirus infection	52/1514	316/14529	0.000575785	Human Diseases	Infectious disease: viral
hsa04916	Melanogenesis	21/1514	95/14529	0.000650055	Organismal Systems	Endocrine system
hsa04933	AGE-RAGE signaling pathway in diabetic complications	21/1514	94/14529	0.000560361	Human Diseases	Endocrine and metabolic disease
hsa04060	Cytokine-cytokine receptor interaction	48/1514	287/14529	0.000639373	Environmental Information Processing	Signaling molecules and interaction
hsa00260	Glycine, serine and threonine metabolism	12/1514	40/14529	0.000543706	Metabolism	Amino acid metabolism
hsa05226	Gastric cancer	28/1514	143/14529	0.000742189	Human Diseases	Cancer: specific types
hsa04923	Regulation of lipolysis in adipocytes	14/1514	54/14529	0.0009868	Organismal Systems	Endocrine system
hsa04218	Cellular senescence	29/1514	153/14529	0.001036158	Cellular Processes	Cell growth and death
hsa04913	Ovarian steroidogenesis	13/1514	49/14529	0.001175034	Organismal Systems	Endocrine system
hsa04390	Hippo signaling pathway	29/1514	154/14529	0.001152336	Environmental Information Processing	Signal transduction
hsa04512	ECM-receptor interaction	19/1514	87/14529	0.001342493	Environmental Information Processing	Signaling molecules and interaction
hsa05224	Breast cancer	27/1514	142/14529	0.001444753	Human Diseases	Cancer: specific types
hsa04210	Apoptosis	24/1514	122/14529	0.001603728	Cellular Processes	Cell growth and death
hsa05323	Rheumatoid arthritis	19/1514	88/14529	0.001548295	Human Diseases	Immune disease

hsa04371	Apelin signaling pathway	25/1514	130/14529	0.001806125	Environmental Information Processing	Signal transduction
hsa04640	Hematopoietic cell lineage	20/1514	96/14529	0.001866334	Organismal Systems	Immune system
hsa04540	Gap junction	18/1514	83/14529	0.001929823	Cellular Processes	Cellular community - eukaryotes
hsa03460	Fanconi anemia pathway	13/1514	51/14529	0.001749981	Genetic Information Processing	Replication and repair
hsa04510	Focal adhesion	33/1514	189/14529	0.002071286	Cellular Processes	Cellular community - eukaryotes
hsa04024	cAMP signaling pathway	36/1514	212/14529	0.002197327	Environmental Information Processing	Signal transduction
hsa05417	Lipid and atherosclerosis	34/1514	199/14529	0.002588003	Human Diseases	Cardiovascular disease
hsa05166	Human T-cell leukemia virus 1 infection	35/1514	207/14529	0.002700318	Human Diseases	Infectious disease: viral
hsa05206	MicroRNAs in cancer	27/1514	149/14529	0.00296295	Human Diseases	Cancer: overview
hsa00140	Steroid hormone biosynthesis	14/1514	60/14529	0.002913851	Metabolism	Lipid metabolism
hsa04668	TNF signaling pathway	21/1514	107/14529	0.003134689	Environmental Information Processing	Signal transduction
hsa04657	IL-17 signaling pathway	18/1514	88/14529	0.003787216	Organismal Systems	Immune system
hsa04115	p53 signaling pathway	15/1514	69/14529	0.004334002	Cellular Processes	Cell growth and death
hsa04061	Viral protein interaction with cytokine and cytokine receptor	19/1514	97/14529	0.004918597	Environmental Information Processing	Signaling molecules and interaction
hsa04611	Platelet activation	22/1514	118/14529	0.004860869	Organismal Systems	Immune system
hsa04713	Circadian entrainment	18/1514	91/14529	0.005482883	Organismal Systems	Environmental adaptation
hsa04610	Complement and coagulation cascades	17/1514	85/14529	0.006100092	Organismal Systems	Immune system
hsa05418	Fluid shear stress and atherosclerosis	23/1514	129/14529	0.007084058	Human Diseases	Cardiovascular disease
hsa05225	Hepatocellular carcinoma	27/1514	160/14529	0.007965148	Human Diseases	Cancer: specific types
hsa04921	Oxytocin signaling pathway	25/1514	145/14529	0.007940541	Organismal Systems	Endocrine system
hsa04360	Axon guidance	29/1514	175/14529	0.007887053	Organismal Systems	Development and regeneration
hsa04912	GnRH signaling pathway	17/1514	87/14529	0.007747341	Organismal Systems	Endocrine system
hsa04970	Salivary secretion	17/1514	88/14529	0.00869554	Organismal Systems	Digestive system
hsa04310	Wnt signaling pathway	27/1514	161/14529	0.008647626	Environmental Information Processing	Signal transduction
hsa05146	Amoebiasis	18/1514	96/14529	0.009649221	Human Diseases	Infectious disease: parasitic
hsa03420	Nucleotide excision repair	10/1514	42/14529	0.009587731	Genetic Information Processing	Replication and repair
hsa05414	Dilated cardiomyopathy	17/1514	90/14529	0.010869469	Human Diseases	Cardiovascular disease

hsa05142	Chagas disease	18/1514	97/14529	0.010727084	Human Diseases	Infectious disease: parasitic
hsa05134	Legionellosis	12/1514	56/14529	0.01139963	Human Diseases	Infectious disease: bacterial
hsa05145	Toxoplasmosis	19/1514	105/14529	0.011629989	Human Diseases	Infectious disease: parasitic
hsa04151	PI3K-Akt signaling pathway	49/1514	340/14529	0.0118826	Environmental Information Processing	Signal transduction
hsa04971	Gastric acid secretion	14/1514	70/14529	0.012157164	Organismal Systems	Digestive system
hsa05214	Glioma	14/1514	71/14529	0.013733361	Human Diseases	Cancer: specific types
hsa03410	Base excision repair	8/1514	32/14529	0.014671116	Genetic Information Processing	Replication and repair
hsa00232	Caffeine metabolism	3/1514	6/14529	0.017730451	Metabolism	Biosynthesis of other secondary metabolites
hsa05212	Pancreatic cancer	14/1514	73/14529	0.017354036	Human Diseases	Cancer: specific types
hsa05207	Chemical carcinogenesis - receptor activation	29/1514	186/14529	0.017652794	Human Diseases	Cancer: overview
hsa04114	Oocyte meiosis	21/1514	125/14529	0.018620901	Cellular Processes	Cell growth and death
hsa04062	Chemokine signaling pathway	28/1514	180/14529	0.020017371	Organismal Systems	Immune system
hsa05210	Colorectal cancer	15/1514	82/14529	0.02122789	Human Diseases	Cancer: specific types
hsa04720	Long-term potentiation	12/1514	61/14529	0.021953503	Organismal Systems	Nervous system
hsa00650	Butanoate metabolism	7/1514	28/14529	0.021907164	Metabolism	Carbohydrate metabolism
hsa04925	Aldosterone synthesis and secretion	16/1514	91/14529	0.025077734	Organismal Systems	Endocrine system
hsa04514	Cell adhesion molecules	23/1514	145/14529	0.026710389	Environmental Information Processing	Signaling molecules and interaction
hsa04064	NF-kappa B signaling pathway	17/1514	99/14529	0.026420315	Environmental Information Processing	Signal transduction
hsa04724	Glutamatergic synapse	18/1514	107/14529	0.027551624	Organismal Systems	Nervous system
hsa00591	Linoleic acid metabolism	7/1514	29/14529	0.026356115	Metabolism	Lipid metabolism
hsa05144	Malaria	10/1514	49/14529	0.027530105	Human Diseases	Infectious disease: parasitic
hsa05022	Pathways of neurodegeneration - multiple diseases	60/1514	453/14529	0.030392643	Human Diseases	Neurodegenerative disease
hsa04750	Inflammatory mediator regulation of TRP channels	16/1514	93/14529	0.030145834	Organismal Systems	Sensory system
hsa00630	Glyoxylate and dicarboxylate metabolism	7/1514	30/14529	0.031382656	Metabolism	Carbohydrate metabolism
hsa00983	Drug metabolism - other enzymes	14/1514	79/14529	0.032599501	Metabolism	Xenobiotics biodegradation and metabolism

hsa04022	cGMP-PKG signaling pathway	24/1514	156/14529	0.033220771	Environmental Information Processing	Signal transduction
hsa05215	Prostate cancer	15/1514	87/14529	0.034430392	Human Diseases	Cancer: specific types
hsa04216	Ferroptosis	8/1514	38/14529	0.039121843	Cellular Processes	Cell growth and death
hsa05133	Pertussis	13/1514	74/14529	0.041010296	Human Diseases	Infectious disease: bacterial
hsa05205	Proteoglycans in cancer	28/1514	193/14529	0.044586975	Human Diseases	Cancer: overview
hsa04625	C-type lectin receptor signaling pathway	16/1514	98/14529	0.046065845	Organismal Systems	Immune system
hsa04974	Protein digestion and absorption	16/1514	99/14529	0.049852935	Organismal Systems	Digestive system